A dynamic Ni(OH)$_2$-NiOOH/NiFeP heterojunction enabling high-performance E-upgrading of hydroxymethylfurfural

Ruipeng Luo [a,b,d], Yuyang Li [c], Lixin Xing [a,b], Ning Wang [a], Ruyi Zhong [a], Zhengyi Qian [b], Chunyu Du [b], Geping Yin [b], Yucheng Wang [c,*], Lei Du [a,b,**]

[a] Huangpu Hydrogen Innovation Center/Guangzhou Key Laboratory for Clean Energy and Materials, School of Chemistry and Chemical Engineering, Guangzhou University, Guangzhou 510006, China
[b] School of Chemistry and Chemical Engineering, Harbin Institute of Technology, Harbin 150001, China
[c] State Key Laboratory of Physical Chemistry of Solid Surfaces, Collaborative Innovation Center of Chemistry for Energy Materials, College of Chemistry and Chemical Engineering, Xiamen University, Xiamen 361005, China
[d] Magnetic Resonance Research Centre, Institute for Molecules and Materials, Faculty of Science, Radboud University, Nijmegen 6525AJ, The Netherlands

ARTICLE INFO

ABSTRACT

Facilely upgrading 5-Hydroxymethylfurfural (HMF) *via* controllable oxidation of aldehyde and hydroxymethyl groups has attracted increasing attention since one of the products, 2,5-Furandicarboxylic acid (FDCA), is of great industrial value. Herein, the surface reconstruction of NiFeP and underlying dynamic Ni(OH)$_2$-NiOOH transformation are characterized under electro-anodic HMF oxidation reaction (HMFOR). The Ni(OH)$_2$-NiOOH/NiFeP heterojunction presents extraordinary HMFOR performance and produces FDCA with a yield over 99% and a Faradaic efficiency over 94%. The reconstructed NiOOH is suggested to chemically (not electrochemically) oxidize HMF while itself is reduced back to Ni(OH)$_2$; The applied anodic potential then drives the oxidation of Ni(OH)$_2$ to NiOOH, to circlize the HMF oxidation process. Meanwhile, the deeper oxidation of NiOOH to NiO(OH)$_2$ or beyond can drive the oxygen evolution reaction (OER). Therefore, a NiOOH-centered dual-circle mechanism is unraveled to understand the entangled and competitive HMFOR and OER, which will be helpful to design better HMFOR electrocatalysts.

1. Introduction

5-Hydroxymethylfurfural (HMF) is a biomass-derived platform chemical, which can be used to produce a variety of value-added products [1,2]. For example, the 2,5-Furandicarboxylic acid (FDCA), generated *via* aldehyde and hydroxymethyl oxidation, is of great economic value and is crowned as one of the twelve most value-added chemicals derived from biomass by the U.S. Department of Energy (DOE) [3,4]. The selective oxidation of HMF to FDCA has been conventionally conducted by high-temperature thermocatalysis [5,6]. Recently, electrochemical oxidation method as an important component of electro-valorization or electro-refinery is emerging as a more promising approach to handle this conversion due to its relatively mild operating conditions [7–10].

So far, versatile non-precious metal electrocatalysts such as phosph-ide [11–13], sulf-ide [14], and nitr-ide [15] (denoted as metal X-ide for convenience) have shown extraordinary performance for HMF oxidation reaction (HMFOR) in alkaline electrolyte. Notably, the metal X-ide catalysts are highly active toward alkaline oxygen evolution reaction (OER) as well [16–19]. Both of the two reactions share an overlapped potential range [17,20]. The competitive OER needs to be suppressed in this regard to increase the Faradaic efficiency of HMFOR. On the other hand, the metal Xides are less stable and tend to be oxidized as the corresponding metal oxide and (oxy)hydroxide under the high anodic potential range [21,22]. For example, the surface reconstruction of metal Xides as OER catalyst have been well documented [19,23,24]. It is thus interesting to ascertain whether the reconstruction takes place or not in HMFOR process with the promising metal Xides as catalysts. Interestingly, the surface reconstruction of metal Xide catalysts may offer benefits to improve the OER kinetics as we reviewed in Ref. [25]. If

---

this process takes place in HMFOR, it is speculated that the *in-situ* generated metal (oxy)hydroxide/Xide heterojunction is helpful in improving the catalytic performance. Therefore, the purpose of this work is to i) identify the possible surface reconstruction process and metal (oxy)hydroxide/Xide heterojunction formation of a representative metal phosphide; ii) investigate the active moieties for HMFOR and competitive OER and iii) explore how to improve HMFOR kinetics and inhibit the competitive OER.

To validate the above hypotheses, we herein employ a typical nickel-iron phosphide (NiFeP) as the "pre-catalyst". It shows high "apparent" catalytic performance in both HMFOR and OER. Its surface reconstruction during HMFOR and OER is monitored by the *in-situ* Raman spectra, as well as other *ex-situ* characterizations. It is found that the *in-situ* formed NiOOH/NiFeP heterojunction (under anodic potential) spontaneously oxidizes HMF in a non-electrochemical (non-EC) way, which is then rapidly reduced backward to Ni(OH)$_2$/NiFeP, forming a dynamic Ni(OH)$_2$-NiOOH circle; For OER, the NiOOH/NiFeP is oxidized as NiO(OH)$_2$/NiFeP and beyond to evolve oxygen. A "NiOOH-centered" dual-circle mechanism can thus be proposed to understand the entangled and competitive HMFOR and OER, which is helpful to guide the catalyst design for HMFOR.

2. Experimental section

2.1. Preparation of NiFeP and NiFe(OH)$_x$ on the nickel foam (NF) substrates

Nickel foam (NF) was first etched with 6 M HCl for 20 min under ultrasonic followed by washing with ethanol and water to remove the oxide on the surface. The electrodeposition of NiFeP and NiFe(OH)$_x$ was carried out in a three-electrode system electrochemical cell. The cleaned nickel foam, an Ag/AgCl (3 M KCl) electrode and a graphite rod were employed as the working electrode, reference electrode, and counter electrode, respectively. To be specific, NiFeP was deposited in an aqueous solution with 3 mM NiSO$_4$.6H$_2$O, 3 mM FeSO$_4$.7H$_2$O, and 36 mM NaH$_2$PO$_2$·H$_2$O by applying −1.0 V *vs* Ag/AgCl for 600 s; NiFe(OH)$_x$ was deposited in an aqueous solution with 3 mM Ni(NO$_3$)$_2$.6H$_2$O and 3 mM Fe(NO$_3$)$_3$.9H$_2$O. NiFeP and Ni(OH)$_2$ by applying −1.0 V *vs* Ag/AgCl for 600 s. After electrodeposition, the NiFeP and NiFe(OH)$_x$ were rinsed with deionized water and dried in air. The nickel foam substrate can be changed to other electronic conductive substrate, *e.g.*, FTO in this work.

2.2. Physical characterization

Field emission-scanning electron microscope (FE-SEM) was carried out on a ZEISS Merlin Compact microscope with 20 kV accelerating voltage. X-ray photoelectron spectroscopy (XPS) was performed on a Thermo ESCALAB 250XI spectrometer. Transmission electron microscope (TEM) and energy dispersive X-ray spectroscopy (EDS) were performed on a JEOL JEM-2100 F microscope at 200 kV. X-ray diffraction (XRD) was performed on a BRUKER AXS instrument. *In-situ* Raman was performed on an Xplora Plus Raman instrument (HORIBA Jobin Yvon) with a 50x objective. The excitation laser lines were 532 nm with a laser power of about 1.5 mW. It took 10 s to acquire one experimental Raman spectrum each time with four accumulations. Raman frequencies were firstly calibrated by using Si wafer (520.6 cm^{-1}) in each experiment. The electrochemical signals were input through the CHI 630E. Hg/HgO electrode and Pt wires were used as reference electrode and counter electrode in Raman electrolytic cell, respectively.

2.3. Electrochemical tests

LSV and CV curves were collected by a CHI 760e (CH Instruments, Inc.) electrochemical workstation at a scan rate of 5 mV s^{-1}. The prepared NiFeP-NF (NiFeP film on nickel foam substrate) electrode as the working electrode, Ag/AgCl (3 M KCl) as the reference electrode, and

graphite electrode as the auxiliary electrode were placed in a three-electrode cell. Potentiostatic oxidation of HMF was carried out in an H-shaped electrochemical cell (Fig. S11). The working electrode was in anode chamber while the Ag/AgCl (3 M KCl) as the reference electrode and graphite electrode as the counter electrode were in cathode chamber. The anode and cathode chambers were filled with 15 mL 1 M KOH + 10 mmol HMF and 15 mL 1 M KOH, respectively. The chambers were separated by a Nafion 117 membrane. The HMFOR was performed at 1.435 V until 86.85 C electron passed.

2.4. Product analysis

To quantitatively analyze the HMF oxidation products after chronoamperometry test at 1.435 V, 20 μL of solution in anode chamber was taken and diluted to 1 mL, which was then transferred and analyzed by High Performance Liquid Chromatography (HPLC, Thermo U3000) equipped with an ultraviolet-visible (UV–VIS) detector at a wavelength of 265 nm and an C18 column at 40 °C. The mobile phase consists of 70% ammonium formate (5 mM) aqueous solution and 30% methanol. The flow rate was set at 0.5 mL min^{-1}. The products were quantitatively analyzed by the external standard method based on the pure intermediates including HMF (Fig. S29a), HMFCA (Fig. S29b), DFF (Fig. S29c), FFCA (Fig. S29d), and FDCA (Fig. S29e).

The conversion of HMF, yields of oxidation products, and Faraday efficiency of FDCA were calculated following the equations:

$$\text{Conversion (\%)} = \frac{\text{mole of consumed HMF}}{\text{mole of initial HMF}} \times 100\%$$

$$\text{Yield (\%)} = \frac{\text{mole of oxidation product}}{\text{mole of initial HMF}} \times 100\%$$

$$\text{Faraday efficiency (\%)} = \frac{6 \times \text{mole of FDCA} \times \text{Faraday constant}}{\text{passed charge}} \times 100\%$$

2.5. Theoretical calculations

The present first principle DFT calculations are performed by Vienna Ab initio Simulation Package (VASP) [26] with the projector augmented wave (PAW) method [27]. The exchange-functional is treated using the generalized gradient approximation (GGA) of Perdew-Burke-Ernzerhof (PBE) [28] functional. The energy cutoff for the plane wave basis expansion was set to 450 eV and the force on each atom less than 0.03 eV/Å was set for convergence criterion of geometry relaxation. The Brillouin zone was sampled with a gamma-centered grid 2 × 2 × 1 through all the computational process. The self-consistent calculations apply a convergence energy threshold of 10^{-6} eV. A 15 Å vacuum space along the z direction was added to avoid the interaction between the two neighboring images.

The DFT + U correction for strong-correlation 3d electrons of transition metal was taken into account, the U-J value of 5.5 for Ni is used [29].

3. Results and discussion

3.1. Surface reconstruction of NiFeP and Ni(OH)$_2$/NiFeP heterojunction

NiFeP catalyst with high reported activity for both HMFOR and OER is selected as a typical metal X-ide catalyst in this work [11,13,30–32]. The NiFeP catalyst is prepared following a reported electrodeposition method on nickel foam (NF) as the substrate, using an electrolyte consisting of NiSO$_4$, FeSO$_4$, and NaH$_2$PO$_2$ (Fig. S1) [33–36]. Compared with the fresh NF substrate (Fig. S2), the electrode after electrodeposition is fully covered by the NiFeP catalyst as observed by the field emission-scanning electron microscopy (FE-SEM) (Fig. S3a). This electrode is denoted as NiFeP-NF. Magnified SEM image suggests a sheet morphology of NiFeP which grows vertically on the NF surface (Fig. S3b). The amount of deposited NiFeP on NF is much less than those using conventional heat treatment and/or solvothermal methods, so that the NiFeP deposition has almost no influence on the active surface area, morphology and electronic conductivity of the electrodes. As shown in

Figs. S4 and S5, the calculated C_{dl} and R_u value for fresh NF are 1.8484 mF cm^{-2} and 1.33 Ω, which are similar with the NiFeP-NF after deposition (C_{dl}: 1.8332 mF cm^{-2} and R_u: 1.39 Ω) [37]. The Ni, Fe, P elements are uniformly distributed on the NiFeP–NF electrode as revealed by the EDS mapping (Fig. S6). Transmission electron microscopy (TEM) image (Figs. 1a and S7a), high-resolution TEM (HRTEM) image (Fig. S7b), selected area electron diffraction (SAED) pattern (inset of Fig. 1a) and XRD pattern (Fig. 1b) of NiFeP all indicate the poor crystallinity of deposited NiFeP. The full and fine (Ni 2p, Fe 2p, P 2p, C 1s and O 1s) XPS spectra of NiFeP catalyst are shown in Figs. 1c and S8. Particularly, the narrow Ni 2p XPS spectrum is deconvoluted and displays two satellite peaks and four prominent peaks (Fig. 1d): the obvious peaks at 870.3 and 852.7 eV are attributed to the Ni-P bonds, whereas those at 873.5 and 855.7 eV are assigned to Ni(OH)$_2$, likely caused by oxygen and water in the air during moving samples to XPS chamber [30,38]. For Fe 2p spectrum, a peak at ~707 eV can be assigned to Fe-P bond (Fig. 1d) [33,39], indicating the formation of metal-phosphorus bonds.

Based on our recent review paper and literature [19,23–25], the surface of metal phosphide, *i.e.*, NiFeP, is expected to reconstruct under harsh anodic conditions like OER, which is also confirmed in this work. As shown in Fig. S9, an amorphous layer is generated on the bulk NiFeP after potentiostatic OER polarization for 1 h in 1 M KOH (compared to the pristine NiFeP in Fig. S7). The surface-sensitive XPS spectra of the post-OER NiFeP also reveal an obvious signal for Ni(OH)$_2$, as well as the significantly suppressed Ni-P signal (Fig. S10), which is distinct from the initial NiFeP (Fig. 1d). In order to investigate whether such process takes place or not under HMFOR, a potentiostatic HMFOR polarization is conducted in 1 M KOH containing 10 mM HMF for 1 h using NiFeP-NF as the electrode. As shown in Fig. 2a, the post-HMFOR NiFeP also shows a typical layered structure, similar to the post-OER NiFeP. The shell layer is amorphous and about 10 nm in thickness as shown by its HRTEM image (Fig. 2b), which is likely due to the oxidized species during HMFOR. The XPS further confirms the surface oxidation of NiFeP under HMFOR. As shown in Fig. 2c, the deconvoluted Ni 2p XPS spectra of post-HMFOR NiFeP not only shows two peaks at 873.3 and 855.7 eV, assigned to Ni(OH)$_2$, but also shows the disappearance of Ni-P [18,40,41]. The failure in detecting Ni-P bond by XPS demonstrates the complete oxidation of NiFeP surface [42]. Since the thickness of surface oxidation layer is about 10 nm as observed in TEM, the post-HMFOR NiFeP is etched by Ar$^+$ sputtering to a depth of ~10 nm prior to another XPS measurement. Interestingly, the in-depth XPS analysis shows clear Ni-P bonds (Fig. 2c) and P 2p spectrum (Fig. 2d) supporting that the interior NiFeP core is unaltered during HMFOR. These results confirm the reconstruction of initial NiFeP under HMFOR polarization and the thus-obtained electrode is denoted as Ni(OH)$_2$/NiFeP-NF.

3.2. HMFOR performance of the surface reconstructed Ni(OH)$_2$/NiFeP-NF electrode

The catalytic activity for HMFOR of Ni(OH)$_2$/NiFeP-NF is evaluated by linear sweep voltammetry (LSV) curves in 1 M KOH with 10 mM HMF electrolyte. As shown in Fig. 3a, the onset potential for HMFOR is 1.22 V (hereinafter with respect to reversible hydrogen electrode, RHE), significantly lower than the competitive OER in 1 M KOH (1.32 V). To achieve the same current density of > 20 mA cm^{-2}, the required overpotential for HMFOR is also much lower than OER by 120–150 mV, indicating the preferential HMFOR than OER on the Ni(OH)$_2$/NiFeP-NF electrode [16]. As shown in Fig. S5, the charge transfer resistance (R_{ct}) for HMFOR of NiFeP-NF (*i.e.*, Ni(OH)$_2$/NiFeP-NF, to be specific) is only 6.24 Ω, pretty lower than NF (84.27 Ω), supporting much faster charge
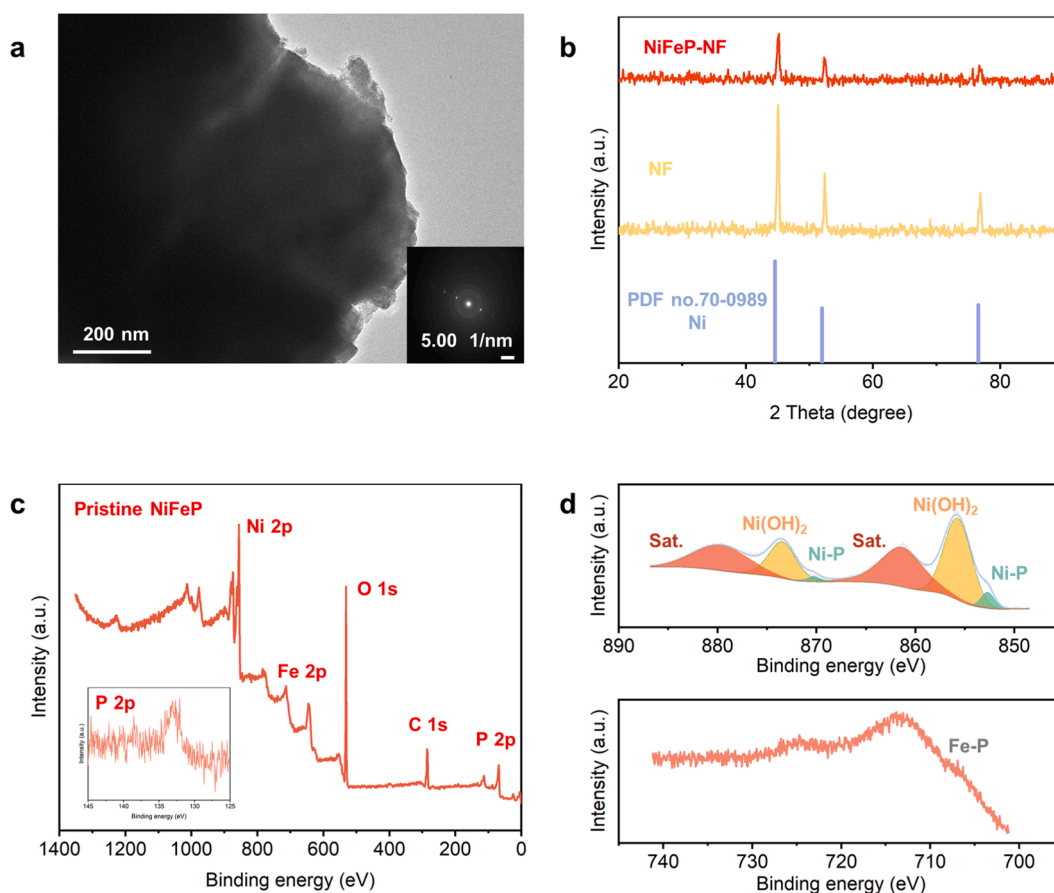

Fig. 1. Physical characterizations of the as-prepared NiFeP-NF. (a) TEM image of NiFeP and its corresponding SEAD. (b) XRD patterns of NiFeP-NF and NF. (c) Full XPS spectrum of NiFeP catalyst. (d) High-resolution Ni 2p and Fe 2p XPS spectra of NiFeP catalyst.
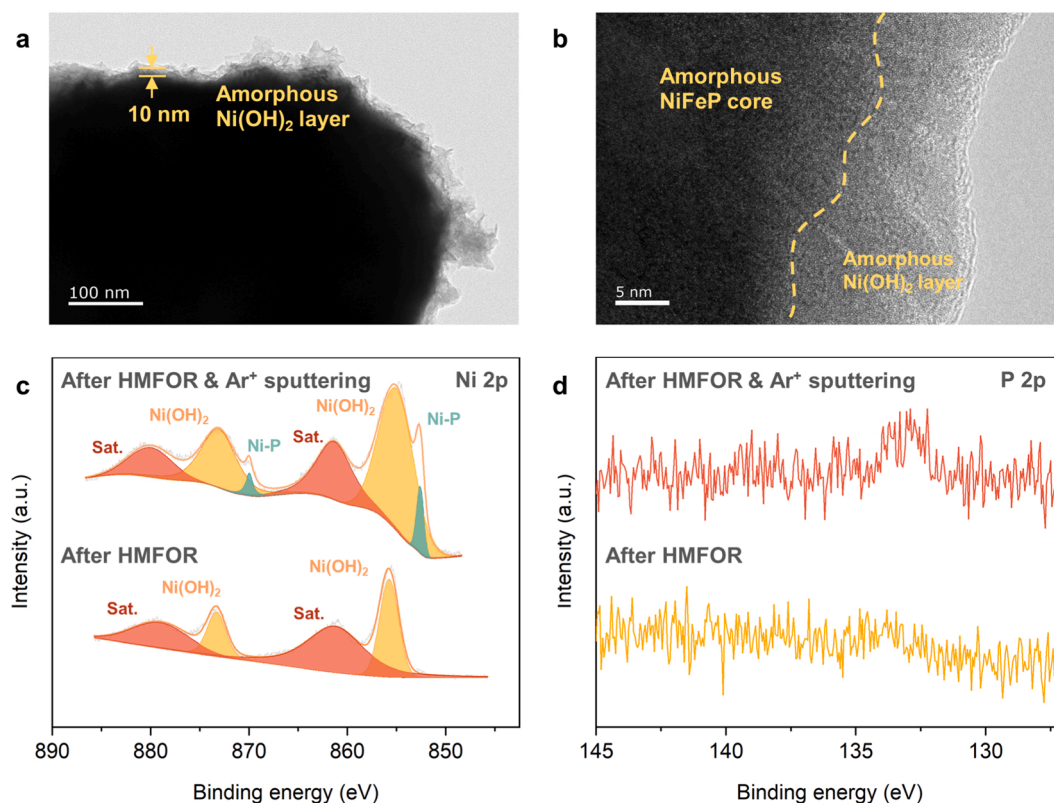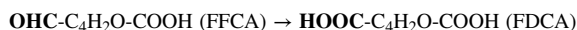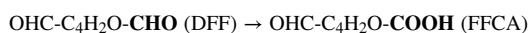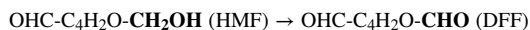
Fig. 2. Physical characterizations of the reconstructed $Ni(OH)_2$/NiFeP after potentiostatic HMFOR polarization. (a) TEM and (b) HRTEM images of $Ni(OH)_2$/NiFeP catalyst. High-resolution (c) Ni 2p and (d) P 2p XPS spectra of $Ni(OH)_2$/NiFeP catalyst before and after Ar^+ sputtering to remove surface oxidation layer.
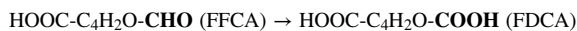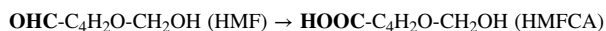
transfer toward HMFOR using NiFeP as the starting catalyst. The product selectivity of HMFOR is evaluated at a constant potential of 1.435 V without iR compensation in a practical H-shaped electrochemical cell (Fig. S11). As shown in Fig. 3b, the HPLC chromatograms of products after different charges passing are illustrated. It is noticed that the HMF in the cell can be completely oxidized after 86.85 C pass (86.85 C electrons are theoretically needed to completely oxidize HMF in the cell), and the FDCA yield is up to 99.4%. It should be noted that the corresponding Faradaic efficiency is 94.62%, which is lower than the yield, indicating that the side reaction takes place, *e.g.*, OER.

The HMF can be oxidized through two pathways (inset of Fig. 3b) [1]: i) hydroxymethyl oxidation and ii) aldehyde oxidation pathways:
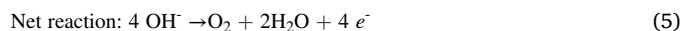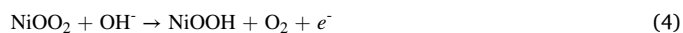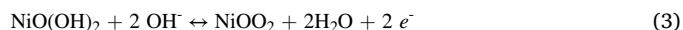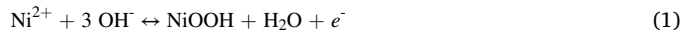
Hydroxymethyl oxidation pathway:

OHC-C_4H_2O-**CH$_2$OH** (HMF) → OHC-C_4H_2O-**CHO** (DFF)

OHC-C_4H_2O-**CHO** (DFF) → OHC-C_4H_2O-**COOH** (FFCA)

OHC-C_4H_2O-COOH (FFCA) → **HOOC**-C_4H_2O-COOH (FDCA)

Aldehyde oxidation pathway:

OHC-C_4H_2O-CH$_2$OH (HMF) → **HOOC**-C_4H_2O-CH$_2$OH (HMFCA)

HOOC-C_4H_2O-**CH$_2$OH** (HMFCA) → HOOC-C_4H_2O-**CHO** (FFCA)

HOOC-C_4H_2O-**CHO** (FFCA) → HOOC-C_4H_2O-**COOH** (FDCA)

By plotting the conversion rate of various products *vs.* charge passing (Fig. S12), no DFF is detected. Therefore, the aldehyde oxidation pathway is confirmed using the $Ni(OH)_2$/NiFeP-NF electrode in this work, which is consistent to most reported non-noble metal catalysts [15,43] In addition, the yields of HMFCA and FFCA are always low, indicating that the conversion of these intermediates to the final product FDCA is fast, thus giving a near 100% selectivity of FDCA on the Ni(OH)$_2$/NiFeP-NF. In following three consecutive test cycles, the Ni

(OH)$_2$/NiFeP-NF electrode maintains stable performance in terms of conversion, yield, and Faradaic efficiency (Figs. 3c, S13, S14, S15) [44]. The above results strongly suggest that the $Ni(OH)_2$/NiFeP-NF is an efficient electrode to catalyze HMFOR and produce FDCA with high selectivity.

So far, we have confirmed that the surface reconstruction and formation of $Ni(OH)_2$ take place under both OER and HMFOR, forming the $Ni(OH)_2$/NiFeP heterojunction. It has been well understood that the surface reconstruction of $Ni(OH)_2$ to NiOOH starts at 1.35 V under OER, which is consistent with the pre-peak (Ni^{2+}/Ni^{3+} redox) at ∼ 1.36 V in Fig. 3a [45,46]. The OER follows four elementary steps on Ni-based catalyst in alkaline electrolyte involving the formation of NiOOH (Eqs. (1)–(4)) [47,48]:

$$Ni^{2+} + 3\ OH^- \leftrightarrow NiOOH + H_2O + e^- \quad (1)$$

$$NiOOH + OH^- \leftrightarrow NiO(OH)_2 + e^- \quad (2)$$

$$NiO(OH)_2 + 2\ OH^- \leftrightarrow NiOO_2 + 2H_2O + 2\ e^- \quad (3)$$

$$NiOO_2 + OH^- \rightarrow NiOOH + O_2 + e^- \quad (4)$$

Net reaction: $4\ OH^- \rightarrow O_2 + 2H_2O + 4\ e^- \quad (5)$

However, the *in-situ* formed NiOOH cannot be accurately identified with *ex-situ* physical characterizations. Therefore, *in-situ* Raman spectroscopy is employed to get more insights into the surface reconstruction process under both HMFOR and OER.

3.3. The dynamic transformation between $Ni(OH)_2$ and NiOOH under HMFOR

The *in-situ* Raman spectra under OER conditions are recorded following potential changes from 1.0 V to 1.55 V and then back to 1.0 V. As shown in Fig. 4a, two peaks at 456 and 520 cm^{-1} are observed at
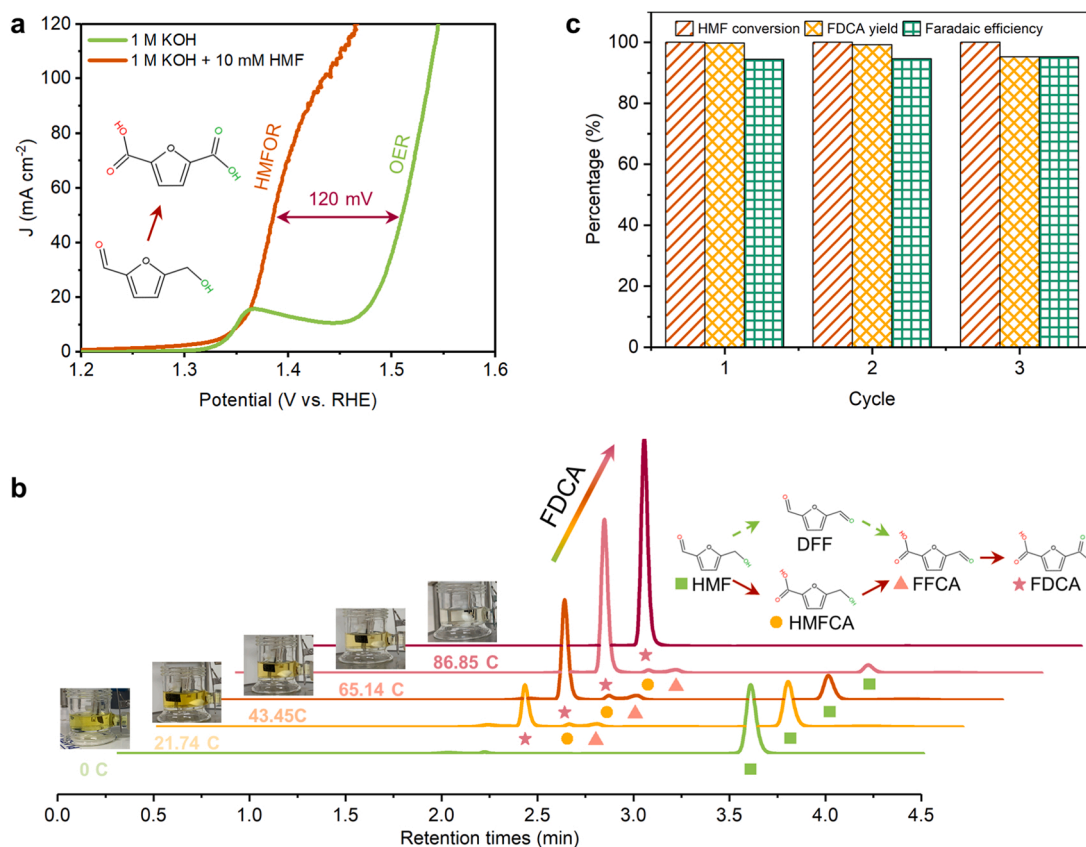
Fig. 3. HMFOR performance of the surface reconstructed Ni(OH)$_2$/NiFeP-NF. (a) LSV curves of Ni(OH)$_2$/NiFeP-NF in 1 M KOH and 1 M KOH + 10 mM HMF. (b) HPLC chromatograms of HMFOR products at 1.435 V after various amounts of charge passed and two possible reaction pathways of HMFOR. (c) HMF conversion, FDCA yield, and Faradaic efficiency in three consecutive test cycles toward HMFOR using Ni(OH)$_2$/NiFeP-NF electrode.
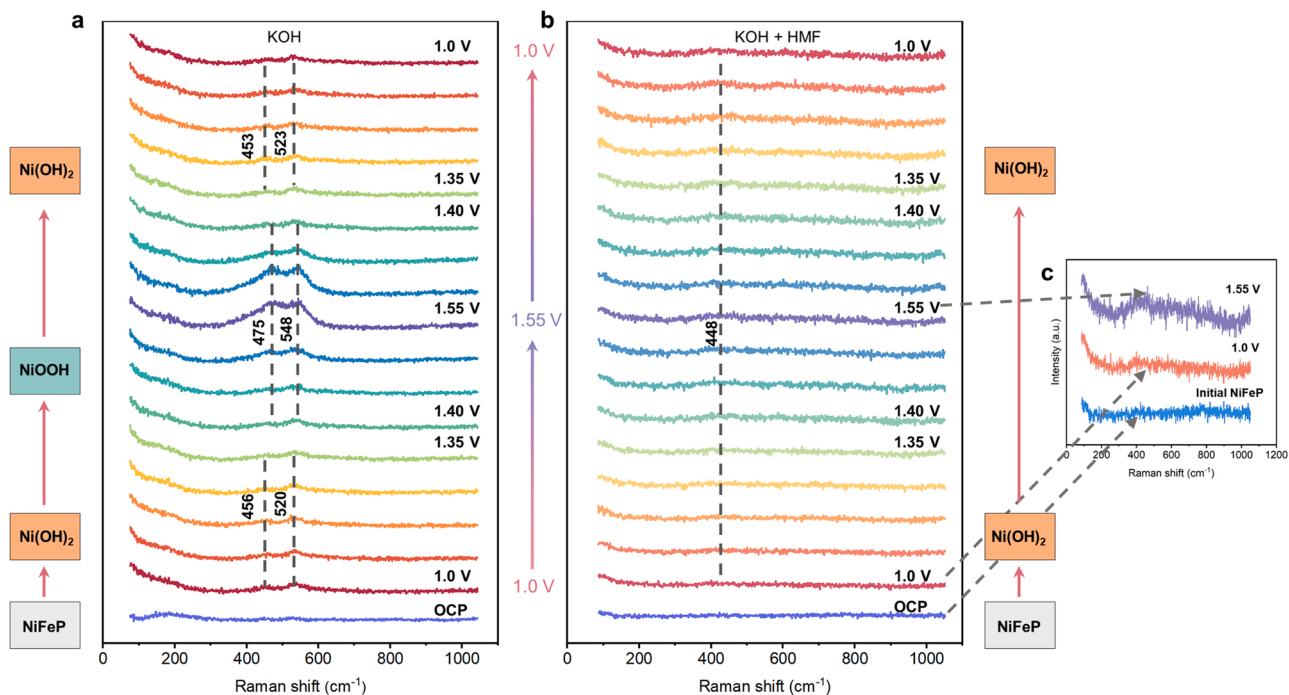

Fig. 4. *In-situ* characterization for the surface reconstruction of NiFeP catalyst. *In-situ* Raman study of NiFeP catalysts during (a) OER in 0.1 M KOH electrolyte and (b) HMFOR in 0.1 M KOH electrolyte with 10 mM HMF. (c) *In-situ* Raman spectra of NiFeP at OCP, 1.0 V, and 1.55 V during the first HMFOR cycle, which are taken from (b).

1.0 V, which are assigned to $Ni(OH)_2$, indicating the reversible reconstruction of NiFeP catalyst. In the potential range of 1.40–1.55 V, these two peaks gradually blue-shift to 475 and 548 cm^{-1}, respectively, with the increase of potential. The peaks at 475 and 548 cm^{-1} are assigned to E_g Ni-O bending vibration and A_{1g} Ni-O stretching vibration in NiOOH [49,50], respectively. Then, when the potential decreases backward from 1.55 V to 1.0 V, the characteristic peaks (475 and 548 cm^{-1}) of NiOOH shift back to those featuring $Ni(OH)_2$ (453 and 523 cm^{-1}). The above results suggest the dynamic transformation of $Ni(OH)_2$ and NiOOH depending on potential [51,52].

Under HMFOR conditions, the *in-situ* Raman results of NiFeP are shown in Fig. 4b and c. Unexpectedly, only a tiny peak at ~ 448 cm^{-1} is observed during three consecutive potential cycles between 1.0 and 1.55 V (Figs. 4b and c, S16, and S17), suggesting the formation of Ni $(OH)_2$ [53], while no signals directly related to the dynamic transformation of $Ni(OH)_2$ and NiOOH under HMFOR (Fig. 4b) are observed. These results are significantly different from the OER study (Fig. 4a).

It is notable that the dynamic transformation does exist during HMFOR although the formation of NiOOH is not observed by *in-situ* Raman. As shown in Fig. 3a, the current density for HMFOR increases rapidly at the potential of 1.36 V where the NiOOH forms in alkaline media (Ni^{2+}/Ni^{3+} redox, see OER), which is also consistent to the results when performing the *in-situ* Raman tests (1.39 V, Fig. S18). This phenomenon is not coincidental because other groups also observe similar results [15,43,54]. Previous literature also reported that the NiOOH thin film was highly active to chemically oxidize HMF and other aldehydes/alcohols [54–56]. Therefore, it is reasonable to assume that the formed NiOOH is rapidly consumed and reduced back to $Ni(OH)_2$, coupling with chemical (non-electrochemical, non-EC) HMF oxidation, probably in a stoichiometrical way (the stoichiometry is not confirmed). That is, once the NiOOH is formed under anodic potential, the further HMFOR is not related to the applied potential. It explains for no visible formation of NiOOH during HMFOR by *in-situ* Raman but clear formation of NiOOH from $Ni(OH)_2$ during OER.

Toward further understanding of the active Ni species during HMFOR, a controlled experiment *in vitro* is performed. The $NiFe(OH)_x$ is directly electrodeposited on NF using the similar procedures except without using NaH_2PO_2 (Fig. S19) [57]. After several cyclic

voltammetry cycles in 1.0 M KOH electrolyte, the surface of hydroxide is transformed to Ni oxyhydroxide layer as expected (black, Fig. S20), which is evidenced by Raman spectra (orange, Fig. S21) [54]. Interestingly, by immersing the as-obtained Ni oxyhydroxide/$NiFe(OH)_x$ electrode in 1.0 M KOH with 10 mM HMF (in the open-circuit state without applied potentials), the black color rapidly fades and the original color of $NiFe(OH)_x$ recovers (Fig. S22a, Supplementary Movie 1) within 1 min. In contrast, the oxyhydroxide does not change in 1.0 M KOH electrolyte without HMF (Fig. S22b, Supplementary Movie 2). This result suggests that the interaction between NiOOH and HMF is a fast spontaneous reaction. In addition, when 1.0 M KOH+ 10 mM HMF is applied in the electrolyte, no NiOOH forms using the same CV procedures (green, Fig. S21). It further corroborates that NiOOH is so rapidly consumed that no signal of NiOOH is observed by *in situ* Raman under HMFOR. Hence, NiOOH is vital in HMFOR and would rapidly oxidize HMF to FDCA.

Based on above results, a reaction mechanism is proposed and shown in Fig. 5a, b. The NiFeP transforms into $Ni(OH)_2$ before 1.36 V; starting from 1.36 V, the $Ni(OH)_2$ is oxidized into NiOOH. In the absence of HMF in the electrolyte, the NiOOH catalyzes the OER following Eqs. (2)–(4) (Fig. 5a). On the other hand, by adding HMF in electrolyte, the *in-situ* formed NiOOH chemically oxidizes HMF ($C_6H_6O_3$), generating FDCA ($C_6H_4O_5$) (Fig. 5b) and itself is fast reduced backward to $Ni(OH)_2$ (Eq. (6)).

$$6\ NiOOH + HMF + 2H_2O \rightarrow 6\ Ni(OH)_2 + FDCA \tag{6}$$

The applied anodic potential then drives $Ni(OH)_2$ transformation into NiOOH (Eq. (7)) to circlize HMF oxidization process.

$$6\ Ni(OH)_2 + 6\ OH^- \leftrightarrow 6\ NiOOH + 6H_2O + 6\ e^- \tag{7}$$
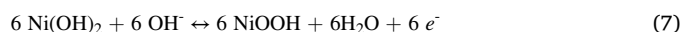
The half-cell anodic reaction for HMF→FDCA can be thus described as Eq. (8) by combining Eqs. (6) and (7):

$$HMF + 6\ OH^- \rightarrow FDCA + 4H_2O + 6\ e^- \tag{8}$$
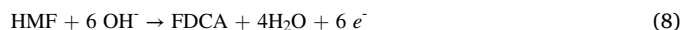
The HMFOR on NiOOH is probably a chemical oxidation process, rather than a surface catalytic process because the HMF conversion (and FDCA production) is almost linear *vs.* charge pass during the whole test
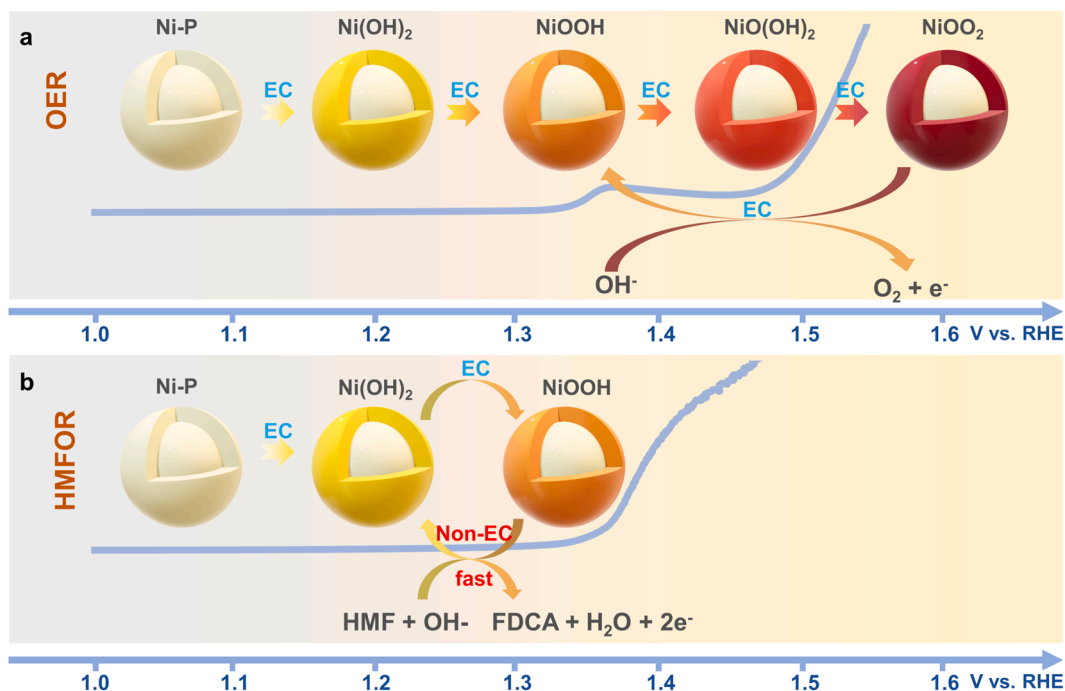

Fig. 5. Schematic illustration of the surface reconstruction and reaction mechanism. Metal phosphide catalyst during (a) the OER and (b) HMFOR process.

(Fig. S12). This means that the conversions of both reactant and product are highly relevant to the consumed electronic energy, *i.e.*, driving repeatable transformation from Ni(OH)$_2$ to NiOOH at anodic potentials.

So far, the dynamic transformation between Ni(OH)$_2$ and NiOOH under HMFOR has been raveled on the reconstructed Ni(OH)$_2$/NiFeP-NF electrode. Furthermore, in order to uncover the extent of surface reconstruction, P 2p XPS spectra are analyzed (Figs. 2c and S10). The post-OER polarization sample shows a P surface composition of 2.79% (Fig. S10), indicating the incomplete surface reconstruction, in contrast to the post-HMFOR polarization sample with almost no visible P signal (Fig. 2c). This result indicates that surface reconstruction in the presence of HMF is more severe and the surface layer is thoroughly oxidized. Such severe surface reconstruction is in align with the proposed dynamic transformation of Ni(OH)$_2$ and NiOOH under HMFOR.

In the *in-situ* Raman measurements, neither the formation of Fe hydroxide nor the reconstruction of Fe species during both OER and HMFOR is observed. XPS results also support that the Fe 2p spectrum in NiFeP-NF almost does not change before and after the HMFOR test as shown in Fig. S23. It has been reported that adding a small amount of Fe to nickel-based catalysts can significantly improve their OER performance [58,59]. Therefore, it is thus interesting to discuss the role of Fe towards HMFOR in this work.

Fe (oxy)hydroxide itself has no contribution to HMFOR, since FeP-FTO (replacing NF by FTO to exclude the possible contribution of NF) is almost inactive toward HMFOR (Fig. S24), which is in consistent with the literature report that FeOOH film shows no catalytic activity for HMFOR [54]. Therefore, the active moiety for HMFOR in NiFeP is Ni species (NiOOH, to be specified), rather than Fe species. Notably, as shown in Fig. S25, tuning the Ni-Fe ratio from 2:1–1:2 does not significantly change both OER and HMFOR performances, but the HMFOR performance of NiP-NF (Fig. S26) is much lower than NiFeP-NF, indicating significantly promotion effects of Fe, similar to the counterpart cases for OER [60]. The synergy between Fe and Ni has been reported to lie in the promotion of high-valence Ni^{4+} [59] and Ni^{3+} [48] for OER. Fe is speculated to exert such a synergistic role as well under HMFOR.

The above experimental results present the surface reconstruction of starting NiFeP into Ni(OH)$_2$/NiFeP, which further undergoes the dynamic transformation between Ni(OH)$_2$ and NiOOH under anodic potential for HMFOR. The NiOOH thus plays as the central role for both HMFOR and OER. A dual-circle mechanism is proposed in Fig. 6a to understand the HMFOR and competitive OER (preferred to be suppressed). Theoretically, the NiOOH presents a more negative adsorption energy for HMF molecules (E_{ads} = −1.81 eV) than OH$^-$ (E_{ads} = −1.40 eV) and H$_2$O (E_{ads} = −0.83 eV) (Fig. S27), indicating a stronger interaction between NiOOH with HMF. Therefore, in the alkaline electrolyte with HMF, the *in-situ* formed NiOOH preferentially adsorbs HMF molecules. If the reaction between HMF and NiOOH is fast enough, the OER will not take place because the formed NiOOH is immediately reduced for HMFOR (*i.e.*, Eqs. (2)–(4) for OER are terminated). However, if the overpotential is high enough or HMF amount is insufficient on the local surface (*e.g.,* limited by mass transfer issue), it is expected that the unconsumed part of NiOOH will be oxidized into higher valence nickel oxides (NiO(OH)$_2$, or even NiOO$_2$), OER will start to take place and even dominates. Therefore, to suppress the side OER, an appropriate potential needs to be chosen for the formation of active metal oxyhydroxide and the avoidance of the too-high valence species, and the local HMF
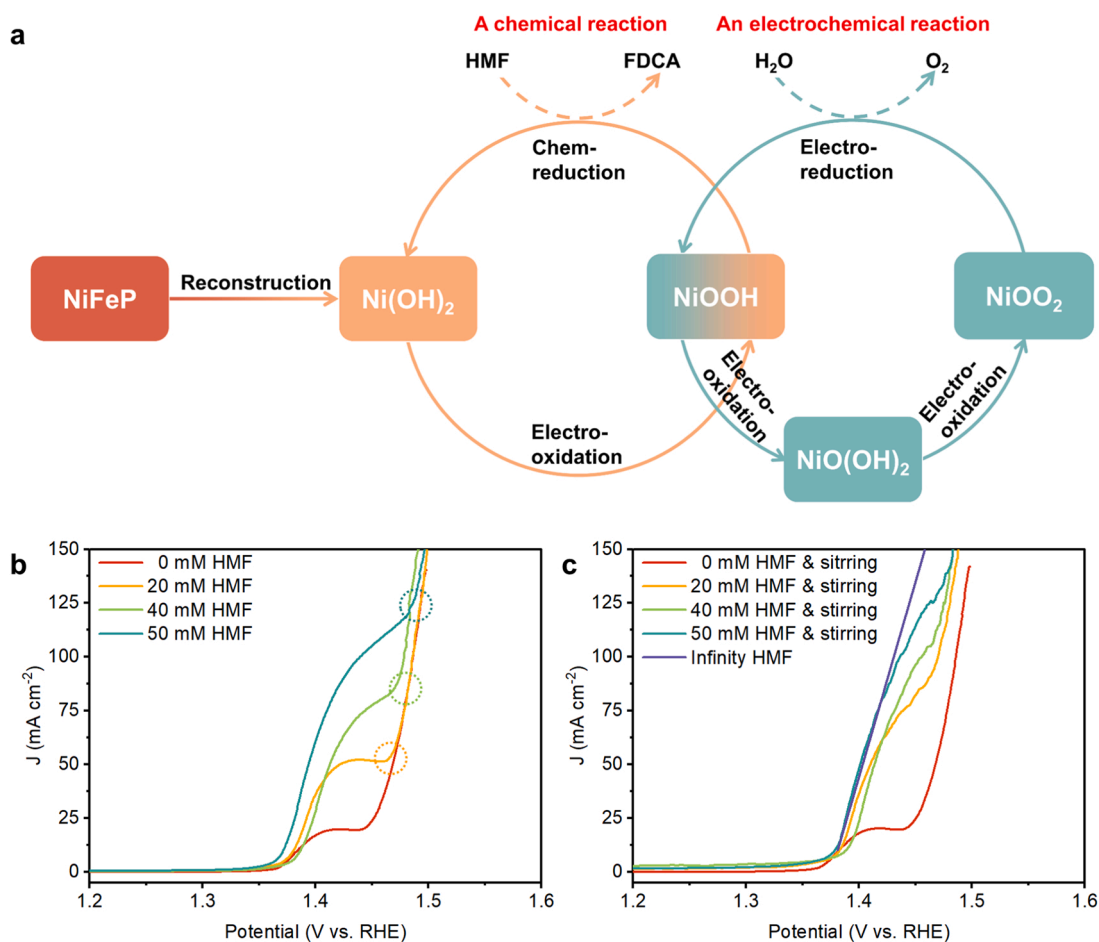

Fig. 6. The dual-circle mechanism and how to suppress competitive OER. (a) A schematic diagram of the oxyhydroxide-centered dual-cycle mechanism for competitive OER and HMFOR. LSV curves of NiFeP-NF in electrolytes with different HMF concentrations (b) without and (c) with stirring.

transportation needs to be considered as well.

The competitive OER is related to the Faradaic efficiency of HMFOR. By applying a relatively low potential, the FE for HMFOR can be as high as 100%. Nevertheless, low overpotential means low electrochemical reaction rate, while high reaction rate is meaningful for scaling-up of the electrochemical HMFOR. Without stirring, the LSV curves in 1 M KOH with and without HMF where the two curves are overlapped at high potential range (Fig. 6b)—at this point, the local HMF is insufficient (within the diffusion-control region) and OER starts to dominate. By further increasing the HMF concentration in the electrolyte, the point for the two curves to overlap shifts positively (Fig. 6b). The higher HMF concentration provides more HMF on the local surface, which suppresses the OER. With stirring to increase the mass transfer, the overlapping point also shifts more positively for HMFOR (Fig. 6c). In contrast, for OER, the stirring has no influence on the curve (Fig. S28).

4. Conclusion

In summary, the reconstruction of surficial NiFeP to Ni(OH)$_2$ and a dynamic Ni(OH)$_2$-NiOOH/NiFeP heterojunction is investigated during HMFOR. The failure in detecting formed NiOOH by *in-situ* Raman is due to the immediate and spontaneous chemical reaction between HMF and NiOOH that rapidly consumes NiOOH. If the local HMF is insufficient or absent, *i.e.*, at a high overpotential or within a low mass transfer region, the retained NiOOH will be oxidized to higher valence level Ni$^{3+\delta}$ species, which can trigger OER. A reaction mechanism is thus proposed for the competitive HMFOR and OER on metal Xide type catalysts and beyond. Metal oxyhydroxide moiety should be considered as the activity origin and should provide abundant channels to improve mass transport of local HMF. Furthermore, other metal Xide catalysts probably exhibit the similar surface transformation behavior as metal phosphides during HMFOR in this work. Therefore, it is interesting if the same mechanisms work for other metal Xide catalysts during HMFOR, which requires more investigations in the future. These new insights can be helpful in designing advanced metal-based catalysts, to improve the HMFOR kinetics at low overpotentials and enhance selectivity towards FDCA at high overpotentials by suppressing OER.

CRediT authorship contribution statement

Ruipeng Luo: Investigation, Data analysis, Writing – original draft, Writing – review & editing. **Yuyang Li**: Methodology, Calculation, Data analysis, Writing – review & editing. **Lixin Xing**: Visualization, Writing – review & editing. **Ning Wang**: Visualization, Writing – review & editing. **Ruyi Zhong**: Visualization, Writing – review & editing. **Zhengyi Qian**: Visualization, Writing – review & editing. **Chunyu Du**: Visualization, Writing – review & editing. **Geping Yin**: Visualization, Writing – review & editing. **Yucheng Wang**: Resources, Methodology, Visualization, Writing – review & editing. **Lei Du**: Conceptualization, Supervision, Writing – original draft, Writing – review & editing.

Declaration of Competing Interest

The authors declare that they have no known competing financial interests or personal relationships that could have appeared to influence the work reported in this paper.

Acknowledgements

Author contributions

R. Luo and Y. Li contributed equally to this work.

Appendix A. Supplementary material

Supplementary data associated with this article can be found in the online version at doi:10.1016/j.apcatb.2022.121357.

References

[1] Y. Kwon, K.J.P. Schouten, J.C. van der Waal, E. de Jong, M.T.M. Koper, Electrocatalytic conversion of furanic compounds, ACS Catal. 6 (2016) 6704–6717.

[2] J.J. Bozell, G.R. Petersen, Technology development for the production of biobased products from biorefinery carbohydrates—the US Department of Energy's "Top 10″ revisited, Green Chem. 12 (2010) 539.

[3] L. Hu, A.Y. He, X.Y. Liu, J. Xia, J.X. Xu, S.Y. Zhou, J.M. Xu, Biocatalytic transformation of 5-hydroxymethylfurfural into high-value derivatives: recent advances and future aspects, ACS Sustain. Chem. Eng. 6 (2018) 15915–15935.

[4] X.L. Tong, Y. Ma, Y.D. Li, Biomass into chemicals: conversion of sugars to furan derivatives by catalytic processes, Appl. Catal. A Gen. 385 (2010) 1–13.

[5] X.W. Han, C.Q. Li, Y. Guo, X.H. Liu, Y.G. Zhang, Y.Q. Wang, N-doped carbon supported Pt catalyst for base-free oxidation of 5-hydroxymethylfurfural to 2,5-furandicarboxylic acid, Appl. Catal. A Gen. 526 (2016) 1–8.

[6] Y.Y. Gorbanev, S. Kegaens, A. Riisager, Effect of support in heterogeneous ruthenium catalysts used for the selective aerobic oxidation of HMF in water, Top. Catal. 54 (2011) 1318–1324.

[7] C. Tang, Y. Zheng, M. Jaroniec, S.Z. Qiao, Electrocatalytic refinery for sustainable production of fuels and chemicals, Angew. Chem. Int. Ed. Engl. 60 (2021) 19572–19590.

[8] L. Du, Y.Y. Shao, J.M. Sun, G.P. Yin, C.Y. Du, Y. Wang, Electrocatalytic valorisation of biomass derived chemicals, Catal. Sci. Technol. 8 (2018) 3216–3232.

[9] R. Li, K. Xiang, Z. Peng, Y. Zou, S. Wang, Recent advances on electrolysis for simultaneous generation of valuable chemicals at both anode and cathode, Adv. Energy Mater. 11 (2021).

[10] T. Wang, L. Tao, X. Zhu, C. Chen, W. Chen, S. Du, Y. Zhou, B. Zhou, D. Wang, C. Xie, P. Long, W. Li, Y. Wang, R. Chen, Y. Zou, X.-Z. Fu, Y. Li, X. Duan, S. Wang, Combined anodic and cathodic hydrogen production from aldehyde oxidation and hydrogen evolution reaction, Nat. Catal. (2021).

[11] B. You, N. Jiang, X. Liu, Y. Sun, Simultaneous H2 generation and biomass upgrading in water by an efficient noble-metal-free bifunctional electrocatalyst, Angew. Chem. Int. Ed. Engl. 55 (2016) 9913–9917.

[12] N. Jiang, B. You, R. Boonstra, I.M.T. Rodriguez, Y.J. Sun, Integrating electrocatalytic 5-hydroxymethylfurfural oxidation and hydrogen production via Co-P-derived electrocatalysts, ACS Energy Lett. 1 (2016) 386–390.

[13] G. Yang, Y. Jiao, H. Yan, Y. Xie, A. Wu, X. Dong, D. Guo, C. Tian, H. Fu, Interfacial engineering of MoO2 -FeP heterojunction for highly efficient hydrogen evolution coupled with biomass electrooxidation, Adv. Mater. 32 (2020), e2000455.

[14] B. You, X. Liu, N. Jiang, Y. Sun, A general strategy for decoupled hydrogen production from water splitting by integrating oxidative biomass valorization, J. Am. Chem. Soc. 138 (2016) 13639–13646.

[15] N. Zhang, Y. Zou, L. Tao, W. Chen, L. Zhou, Z. Liu, B. Zhou, G. Huang, H. Lin, S. Wang, Electrochemical oxidation of 5-hydroxymethylfurfural on nickel nitride/carbon nanosheets: reaction pathway determined by in situ sum frequency generation vibrational spectroscopy, Angew. Chem. Int. Ed. Engl. 58 (2019) 15895–15903.

[16] W.J. Liu, L.N. Dang, Z.R. Xu, H.Q. Yu, S. Jin, G.W. Huber, Electrochemical oxidation of 5-hydroxymethylfurfural with NiFe layered double hydroxide (LDH) nanosheet catalysts, ACS Catal. 8 (2018) 5533–5541.

[17] Y.X. Lu, C.L. Dong, Y.C. Huang, Y.Q. Zou, Y.B. Liu, Y.Y. Li, N.N. Zhang, W. Chen, L. Zhou, H.Z. Lin, S.Y. Wang, Hierarchically nanostructured NiO-Co3O4 with rich interface defects for the electro-oxidation of 5-hydroxymethylfurfural, Sci. China Chem. 63 (2020) 980–986.

[18] G. Zhang, Y.S. Feng, W.T. Lu, D. He, C.Y. Wang, Y.K. Li, X.Y. Wang, F.F. Cao, Enhanced catalysis of electrochemical overall water splitting in alkaline media by Fe doping in Ni3S2 nanosheet arrays, ACS Catal. 8 (2018) 5431–5441.

[19] L.A. Stern, L.G. Feng, F. Song, X.L. Hu, Ni2P as a Janus catalyst for water splitting: the oxygen evolution activity of Ni2P nanoparticles, Energy Environ. Sci. 8 (2015) 2347–2351.

[20] X. Huang, J.L. Song, M.L. Hua, Z.B. Xie, S.S. Liu, T.B. Wu, G.Y. Yang, B.X. Han, Enhancing the electrocatalytic activity of CoO for the oxidation of 5-hydroxymethylfurfural by introducing oxygen vacancies, Green Chem. 22 (2020) 843–849.

[21] S. Jin, Are metal chalcogenides, nitrides, and phosphides oxygen evolution catalysts or bifunctional catalysts? ACS Energy Lett. 2 (2017) 1937–1938.

[22] B.R. Wygant, K. Kawashima, C.B. Mullins, Catalyst or precatalyst? The effect of oxidation on transition metal carbide, pnictide, and chalcogenide oxygen evolution catalysts, ACS Energy Lett. 3 (2018) 2956–2966.

[23] C.Y. Yan, J.W. Huang, C.Y. Wu, Y.Y. Li, Y.C. Tan, L.Y. Zhang, Y.H. Sun, X.N. Huang, J. Xiong, In-situ formed NiS/Ni coupled interface for efficient oxygen evolution and hydrogen evolution, J. Mater. Sci. Technol. 42 (2020) 10–16.

[24] K. Xu, P. Chen, X. Li, Y. Tong, H. Ding, X. Wu, W. Chu, Z. Peng, C. Wu, Y. Xie, Metallic nickel nitride nanosheets realizing enhanced electrochemical water oxidation, J. Am. Chem. Soc. 137 (2015) 4119–4125.

[25] R. Luo, Z. Qian, L. Xing, C. Du, G. Yin, S. Zhao, L. Du, Re-looking into the active moieties of metal X-ides (X- = phosph-, sulf-, nitr-, and carb-) toward oxygen evolution reaction, Adv. Funct. Mater. 31 (2021), 2102918.

[26] G. Kresse, J. Furthmuller, Efficiency of ab-initio total energy calculations for metals and semiconductors using a plane-wave basis set, Comput. Mater. Sci. 6 (1996) 15–50.

[27] P.E. Blochl, Projector augmented-wave method, Phys. Rev. B Condens. Matter 50 (1994) 17953–17979.

[28] J.P. Perdew, J.A. Chevary, S.H. Vosko, K.A. Jackson, M.R. Pederson, D.J. Singh, C. Fiolhais, Atoms, molecules, solids, and surfaces: applications of the generalized gradient approximation for exchange and correlation, Phys. Rev. B Condens. Matter 46 (1992) 6671–6687.

[29] C. Lin, Y. Zhao, H. Zhang, S. Xie, Y.F. Li, X. Li, Z. Jiang, Z.P. Liu, Accelerated active phase transformation of NiO powered by Pt single atoms for enhanced oxygen evolution reaction, Chem. Sci. 9 (2018) 6803–6812.

[30] P.F. Liu, X. Li, S. Yang, M.Y. Zu, P.R. Liu, B. Zhang, L.R. Zheng, H.J. Zhao, H. G. Yang, Ni2P(O)/Fe2P(O) interface can boost oxygen evolution electrocatalysis, ACS Energy Lett. 2 (2017) 2257–2263.

[31] F. Hu, S. Zhu, S. Chen, Y. Li, L. Ma, T. Wu, Y. Zhang, C. Wang, C. Liu, X. Yang, L. Song, X. Yang, Y. Xiong, Amorphous metallic NiFeP: a conductive bulk material achieving high activity for oxygen evolution reaction in both alkaline and acidic media, Adv. Mater. 29 (2017), 1606570.

[32] M. Miao, R.Z. Hou, R.J. Qi, Y. Yan, L.Q. Gong, K. Qi, H.F. Liu, B.Y. Xia, Surface evolution and reconstruction of oxygen-abundant FePi/NiFeP synergy in NiFe phosphides for efficient water oxidation, J. Mater. Chem. A 7 (2019) 18925–18931.

[33] J. Shi, F. Qiu, W. Yuan, M. Guo, C. Yuan, Z.-H. Lu, Novel electrocatalyst of nanoporous FeP cubes prepared by fast electrodeposition coupling with acid-etching for efficient hydrogen evolution, Electrochim. Acta 329 (2020), 135185.

[34] M. Das, N. Jena, T. Purkait, N. Kamboj, A. De Sarkar, R.S. Dey, Single-phase Ni5P4-copper foam superhydrophilic and aerophobic core-shell nanostructures for efficient hydrogen evolution reaction, J. Mater. Chem. A 7 (2019) 23989–23999.

[35] C. Tang, A.M. Asiri, Y.L. Luo, X.P. Sun, Electrodeposited Ni-P alloy nanoparticle films for efficiently catalyzing hydrogen- and oxygen-evolution reactions, ChemNanoMat 1 (2015) 558–561.

[36] Q. Liu, S. Gu, C.M. Li, Electrodeposition of nickel-phosphorus nanoparticles film as a Janus electrocatalyst for electro-splitting of water, J. Power Sources 299 (2015) 342–346.

[37] L. Du, L. Luo, Z. Feng, M. Engelhard, X. Xie, B. Han, J. Sun, J. Zhang, G. Yin, C. Wang, Y. Wang, Y. Shao, Nitrogen–doped graphitized carbon shell encapsulated NiFe nanoparticles: a highly durable oxygen evolution catalyst, Nano Energy 39 (2017) 245–252.

[38] C. Tang, R. Zhang, W. Lu, Z. Wang, D. Liu, S. Hao, G. Du, A.M. Asiri, X. Sun, Energy-saving electrolytic hydrogen generation: Ni2 P nanoarray as a high-performance non-noble-metal electrocatalyst, Angew. Chem. Int. Ed. Engl. (2017) 842–846.

[39] Z.-p Lu, L. Sepunaru, Electrodeposition of iron phosphide film for hydrogen evolution reaction, Electrochim. Acta 363 (2020), 137167.

[40] B. Konkena, J. Masa, A.J.R. Botz, I. Sinev, W. Xia, J. Koßmann, R. Drautz, M. Muhler, W. Schuhmann, Metallic NiPS3@NiOOH core–shell heterostructures as highly efficient and stable electrocatalyst for the oxygen evolution reaction, ACS Catal. 7 (2016) 229–237.

[41] B. Song, K. Li, Y. Yin, T. Wu, L.N. Dang, M. Caban-Acevedo, J.C. Han, T.L. Gao, X. J. Wang, Z.H. Zhang, J.R. Schmidt, P. Xu, S. Jin, Tuning mixed nickel iron phosphosulfide nanosheet electrocatalysts for enhanced hydrogen and oxygen evolution, ACS Catal. 7 (2017) 8549–8557.

[42] Y.P. Zhu, H.C. Chen, C.S. Hsu, T.S. Lin, C.J. Chang, S.C. Chang, L.D. Tsai, H. M. Chen, Operando unraveling of the structural and chemical stability of P-substituted CoSe2 electrocatalysts toward hydrogen and oxygen evolution reactions in alkaline electrolyte, ACS Energy Lett. 4 (2019) 987–994.

[43] S. Barwe, J. Weidner, S. Cychy, D.M. Morales, S. Dieckhofer, D. Hiltrop, J. Masa, M. Muhler, W. Schuhmann, Electrocatalytic oxidation of 5-(hydroxymethyl) furfural using high-surface-area nickel boride, Angew. Chem. Int. Ed. Engl. 57 (2018) 11460–11464.

[44] Y. Lu, C.L. Dong, Y.C. Huang, Y. Zou, Z. Liu, Y. Liu, Y. Li, N. He, J. Shi, S. Wang, Identifying the geometric site dependence of spinel oxides for the electrooxidation of 5-hydroxymethylfurfural, Angew. Chem. Int. Ed. Engl. 59 (2020) 19215–19221.

[45] H.M. Sun, X.B. Xu, Z.H. Yan, X. Chen, F.Y. Cheng, P.S. Weiss, J. Chen, Porous multishelled Ni2P hollow microspheres as an active electrocatalyst for hydrogen and oxygen evolution, Chem. Mater. 29 (2017) 8539–8547.

[46] M. Shalom, D. Ressnig, X.F. Yang, G. Clavel, T.P. Fellinger, M. Antonietti, Nickel nitride as an efficient electrocatalyst for water splitting, J. Mater. Chem. A 3 (2015) 8171–8177.

[47] K. Juodkazis, J. Juodkazyte, R. Vilkauskaite, V. Jasulaitiene, Nickel surface anodic oxidation and electrocatalysis of oxygen evolution, J. Solid State Electrochem. 12 (2008) 1469–1479.

[48] X. Zheng, B. Zhang, P. De Luna, Y. Liang, R. Comin, O. Voznyy, L. Han, F.P. Garcia de Arquer, M. Liu, C.T. Dinh, T. Regier, J.J. Dynes, S. He, H.L. Xin, H. Peng, D. Prendergast, X. Du, E.H. Sargent, Theory-driven design of high-valence metal sites for water oxidation confirmed using in situ soft X-ray absorption, Nat. Chem. 10 (2018) 149–154.

[49] J. Huang, Y. Li, Y. Zhang, G. Rao, C. Wu, Y. Hu, X. Wang, R. Lu, Y. Li, J. Xiong, Identification of key reversible intermediates in self-reconstructed nickel-based hybrid electrocatalysts for oxygen evolution, Angew. Chem. Int. Ed. Engl. 58 (2019) 17458–17464.

[50] Y.L. Lo, B.J. Hwang, In situ Raman studies on cathodically deposited nickel hydroxide films and electroless Ni-P electrodes in 1 M KOH solution, Langmuir 14 (1998) 944–950.

[51] J. Herranz, J. Durst, E. Fabbri, A. Patru, X. Cheng, A.A. Permyakova, T.J. Schmidt, Interfacial effects on the catalysis of the hydrogen evolution, oxygen evolution and CO2-reduction reactions for (co-)electrolyzer development, Nano Energy 29 (2016) 4–28.

[52] H. Bode, K. Dehmelt, J. Witte, Zur kenntnis der nickelhydroxidelektrode—I.Über das nickel (II)-hydroxidhydrat, Electrochim. Acta 11 (1966) 1079–1087.

[53] H.B. Li, M.H. Yu, F.X. Wang, P. Liu, Y. Liang, J. Xiao, C.X. Wang, Y.X. Tong, G. W. Yang, Amorphous nickel hydroxide nanospheres with ultrahigh capacitance and energy density as electrochemical pseudocapacitor materials, Nat. Commun. 4 (2013) 1894.

[54] B.J. Taitt, D.-H. Nam, K.-S. Choi, A comparative study of nickel, cobalt, and iron oxyhydroxide anodes for the electrochemical oxidation of 5-hydroxymethylfurfural to 2,5-furandicarboxylic acid, ACS Catal. 9 (2018) 660–670.

[55] M.T. Bender, Y.C. Lam, S. Hammes-Schiffer, K.S. Choi, Unraveling two pathways for electrochemical alcohol and aldehyde oxidation on NiOOH, J. Am. Chem. Soc. 142 (2020) 21538–21547.

[56] W. Chen, C. Xie, Y.Y. Wang, Y.Q. Zou, C.L. Dong, Y.C. Huang, Z.H. Xiao, Z.X. Wei, S.Q. Du, C. Chen, B. Zhou, J.M. Ma, S.Y. Wang, Activity origins and design principles of nickel-based catalysts for nucleophile electrooxidation, Chem 6 (2020) 2974–2993.

[57] X. Lu, C. Zhao, Electrodeposition of hierarchically structured three-dimensional nickel-iron electrodes for efficient oxygen evolution at high current densities, Nat. Commun. 6 (2015) 6616.

[58] L. Trotochaud, S.L. Young, J.K. Ranney, S.W. Boettcher, Nickel-iron oxyhydroxide oxygen-evolution electrocatalysts: the role of intentional and incidental iron incorporation, J. Am. Chem. Soc. 136 (2014) 6744–6753.

[59] N. Li, D.K. Bediako, R.G. Hadt, D. Hayes, T.J. Kempa, F. von Cube, D.C. Bell, L. X. Chen, D.G. Nocera, Influence of iron doping on tetravalent nickel content in catalytic oxygen evolving films, Proc. Natl. Acad. Sci. USA 114 (2017) 1486–1491.

[60] D. Friebel, M.W. Louie, M. Bajdich, K.E. Sanwald, Y. Cai, A.M. Wise, M.J. Cheng, D. Sokaras, T.C. Weng, R. Alonso-Mori, R.C. Davis, J.R. Bargar, J.K. Norskov, A. Nilsson, A.T. Bell, Identification of highly active Fe sites in (Ni,Fe)OOH for electrocatalytic water splitting, J. Am. Chem. Soc. 137 (2015) 1305–1313.